Water Resources Research

RESEARCH ARTICLE
10.1029/2022WR032168

Solute Transport in a Doublet-Type Flow Configuration Through a Weakly Heterogeneous Porous Formation

Gerardo Severino[1] and **Francesco De Paola**[2]

[1]Department of Agricultural Science, University of Naples Federico II, Naples, Italy, [2]Department of Civil, Building and Environmental Engineering, University of Naples Federico II, Naples, Italy

Key Points:

- Transport in a doublet flow is investigated by means of the breakthrough curve (BTC) and its moments
- A simple solution is achieved by dealing with a strongly anisotropic heterogeneous formation
- Results are applied to a couple of field-scale transport experiments

Correspondence to:

G. Severino,
gerardo.severino@unina.it

Citation:

Severino, G., & De Paola, F. (2022). Solute transport in a doublet-type flow configuration through a weakly heterogeneous porous formation. *Water Resources Research*, *58*, e2022WR032168. https://doi.org/10.1029/2022WR032168

Received 9 FEB 2022
Accepted 10 JUL 2022

Author Contributions:

Conceptualization: Gerardo Severino
Data curation: Gerardo Severino, Francesco De Paola
Formal analysis: Gerardo Severino
Investigation: Gerardo Severino
Methodology: Gerardo Severino
Resources: Francesco De Paola
Software: Gerardo Severino
Validation: Gerardo Severino
Writing – original draft: Gerardo Severino, Francesco De Paola
Writing – review & editing: Gerardo Severino

Abstract Steady flow generated by an injecting and a pumping well (doublet) takes place in a porous formation where the spatially variable hydraulic conductivity K is modeled as a stationary, lognormal, random field with anisotropic two-point autocorrelation. The latter is characterized by a vertical integral scale, that is, I_v, smaller than the horizontal one, that is, I. A solute, either passive or reactive, is injected in the medium, and we aim at computing the breakthrough curve (BTC) and its moments not only at the recovery (pumping) well, but also at any location between the two wells. The strong coupling between K and the nonuniformity of the flow renders the problem very difficult. Nevertheless, a simple (analytical) solution is obtained by adopting a few assumptions: (a) wells are replaced by lines of singularity, (b) a perturbation solution which regards the variance σ_Y^2 of the log-conductivity $Y = \ln K$ as a perturbation parameter is employed, (c) the study is limited to strongly anisotropic heterogeneous formations (for which the anisotropy ratio $\lambda = I_v/I$ is much smaller than one), and (d) the impact of pore-scale dispersion is neglected. Central for the computation of the BTC is the statistics of the travel time of a fluid particle released at the injecting well and reaching a control plane located at any position x_1 along the distance connecting the two wells. It is shown that the spatial variability of Y acts de facto like a dispersion mechanism: it enhances spreading, especially in the early arrivals. Useful closed form expressions for moments of the travel time along the central trajectory are also obtained. Finally, the theoretical framework presented in this study is applied to two transport experiments in order to compute the second-order (temporal) moment as function of x_1, and therefore to quantify dispersion occurring in the zone delimited by the two wells.

Plain Language Summary Transport takes place between an injecting well and a pumping one through to a porous formation. The controlling parameter is the conductivity which, unlike the classical approach, here is regarded, in line with field findings, as spatially variable. This renders the problem at stake extremely difficult to solve. However, a simple solution is achieved by adopting a few simplifying assumptions, which nevertheless resemble most of the existing aquifers, and therefore it is applicable to numerous real-world situations. It is shown that the proposed solution finds application in the identification of the aquifer's parameters as well as the quantification of efficiency of decontamination procedures. Finally, the theoretical framework is applied to a couple of transport experiments, in order to illustrate (and to quantify) how dispersion process develops in the zone delimited by the two wells.

1. Introduction

Water flow through porous formations plays a crucial role in the propagation of solutes (Dagan, 1989). Generally, such a phenomenon evolves very slowly, therefore making hard (sometimes prohibitive) ex post procedures. Thus, especially in the case of contaminant transport, predicting models become of paramount importance in order to assess (and concurrently to prevent) possible pollution-situations. While transport in uniform mean flow has received a huge amount of theoretical/experimental investigations (see, e.g., Rubin, 2003, and references therein), transport in a doublet-type flow through heterogeneous porous media has attracted lesser attention, its importance in the applications, notwithstanding (Di Dato et al., 2018).

Typically, transport in a dipole flow is used as a diagnostic tool to identify the aquifer's hydraulic parameters. Specifically, a passive scalar is injected through the well, and the breakthrough curve (BTC) is recovered at the pumping well. Then, the matching between experimental data and theoretical BTC leads to the identification of the formation's properties (see Zech et al., 2018, for an updated overview on the topic). This setup is *in principle* the easiest and fastest tool to identify the formation's properties. However, the limitation of its adoption is due to

complexity of the flow and (more important) transport patterns which, in the case of heterogeneous formations, are not fully understood. As a consequence, it is not surprising that a limited number of experimental studies of this type is available in the literature. Not disregarded, transport in a doublet flow is employed to design efficient strategies of cleaning up portions of polluted groundwaters (Di Dato et al., 2018; Severino, 2022). However, the doublet does not account for the entire history of the dispersion between the solute's release and its recovery. This may affect also the identification of the heterogeneity's structure of the formation. In fact, dispersion in the central zone encompasses all the impact of the heterogeneity, and concurrently the match between theoretical BTC and/or moments with their experimental counterparts leads to an identification of the aquifer's parameters more robust than that achieved by means of the recovered BTC, solely. Besides improving the efficiency of the doublet tests, quantification of the dispersion in the strip delimited by the two wells is also useful when one has to select the working flow rate and the distance of the doublet to design remediation strategies (Di Dato et al., 2018).

Classically, transport in a doublet-flow configuration has been studied by regarding the formation as homogeneous (an exhaustive overview of the existing analytical solutions can be found in Bruggeman (1999)). In this case, flow is characterized by streamlines that are portions of circles lying within the horizontal plane (Severino, 2022). The overall resulting effect is a huge difference in the arrival times along different streamlines (Koplik et al., 1994; Kurowski et al., 1994).

Natural porous formations are *as a rule* heterogeneous, with the log-conductivity Y varying in the space by several orders of magnitude (Rubin, 2003). This spatial variability causes enhanced dispersion due to shortcuts through highly conducting inclusions (Fernández-Garcia et al., 2004; Ptak et al., 2004), leading ultimately to earlier (as compared with a homogeneous medium) mass arrivals (Dagan & Indelman, 1999; Koplik et al., 1994; Zech et al., 2018). In order to account for its erratic variations and the associated uncertainty, it is customary to model Y as a stationary, normal, random field, defined completely by the geometric mean $K_G = \exp(\langle Y \rangle)$ (hereafter, the symbol $\langle\rangle$ will denote the ensemble average operator), variance σ_Y^2, and two-point autocorrelation ρ_Y. The latter is anisotropic, with the horizontal integral scale larger than the vertical one.

Transport in heterogeneous porous media is in general determined by the spatial variations of the advective flow-velocity (Dagan, 1989). This is particularly so in radial-type flows (Indelman & Dagan, 1999). In the present study, modeling of transport is carried out in two steps consisting of: (a) deriving the statistics of the travel time for the specific problem and (b) computing the BTC as well as moments. Thus, we consider a system of injecting/pumping wells (of radius r_w) operating at a constant, specific (per unit depth) discharge Q_w within an unbounded porous medium (Figure 1). The wells' axes are at $(-\ell/2, 0, x_3)$ (injecting), and at $(\ell/2, 0, x_3)$ (pumping). A solute is injected, and a body of many particles (plume), migrating toward the pumping well, develops (Figure 1). We aim at characterizing the plume's migration not only at the recovery (pumping) well, but also in the intermediate zone $x_1 \in]-\ell/2, +\ell/2[$. Unlike transport in uniform mean flows (a comprehensive review can be found in Dagan (1989) and Rubin (2003)), much less has been done for transport in a doublet-type flow configuration. In fact, with the exception of the works of Dagan and Indelman (1999) and Zech et al. (2018), which nevertheless limit to the computation of the BTC at the pumping well, we are not aware of any theoretical study aiming at quantifying simultaneously the BTC at the recovery well as well as dispersion in the zone delimited by the two wells. The difficulty is due to the strong coupling between the spatially variable hydraulic conductivity, and the nonuniformity of the flow. In a recent study, Severino (2022) has derived a closed form expression for the second-order (longitudinal) moment in the strip $x_1 \in]-\ell/2, +\ell/2[$. In particular, he has shown that dispersion in a doublet-type configuration is larger than that in a single well-type flow. This effect is due to the flux which, unlike that in a well-type flow, is rapidly increasing even at the recovery, owing to the presence there of another singularity. However, the above study deals only with a passive scalar, and (more important) it can only account for the dispersion within the strip delimited by the two wells.

Before proceeding further, it is worth mentioning that another viable option is by means of Monte Carlo simulations. However, such an avenue is prone of inaccuracies. In fact, in order to account for the strong nonuniformity of the flow field, very dense grids, especially in the tiny region surrounding the wells, are required. This implies a very large number of nodal equations which prevents de facto achieving accurate results (an extended overview can be found in Bianchi et al. (2011), and references therein). On the contrary, analytical solutions provide direct relationships between the controlling parameters and the model output, therefore giving a straightforward physical insight.

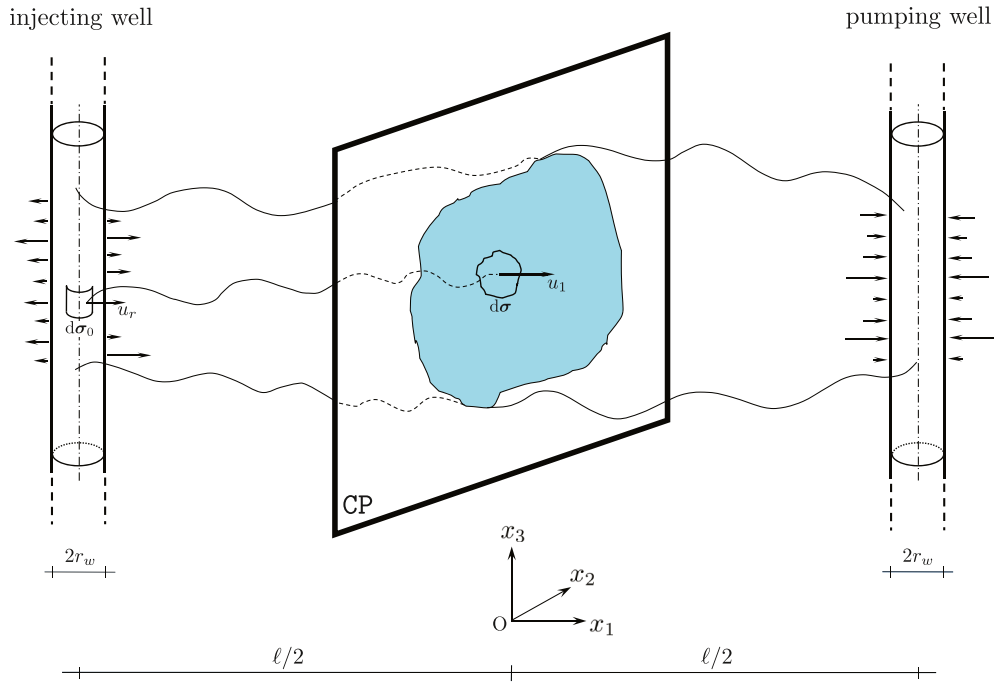

Figure 1. Sketch of a path of a fluid particle starting at the injecting well over a small area $d\boldsymbol{\sigma}_0$ (with velocity u_r), and reaching (with velocity u_1) a control plane (CP) between the two wells.

In the present study, we aim at investigating transport in a dipole-flow configuration by means of temporal moments. The main novelty of the approach is that it allows computing not only the BTC at any location $x_1 \in]-\ell/2, +\ell/2[$ (thus generalizing the study from Dagan and Indelman (1999)), but it also allows quantifying dispersion within the intermediate zone. The paper is organized as follows: we formulate the transport problem in terms of statistics of the travel time (by following the general approach of Cvetkovic and Dagan (1994)); subsequently we derive an approximate (valid for largely anisotropic porous formations) solution for the flow field, that ultimately leads to a simple expression for the BTC, and the associated moments at any x_1. Finally, theoretical results are applied to a couple of field-scale transport experiments in order to provide a quantitative assessment of the dispersion process taking place between the pumping and injecting well. We end up with concluding remarks.

2. Problem Statement

The geometrical set up is that of Figure 1, where we have introduced the spatial coordinate $\boldsymbol{x} \equiv (\boldsymbol{x}_r, x_3)$, being $\boldsymbol{x}_r \equiv (x_1, x_2)$ the coordinate in the horizontal plane. The log-conductivity $Y \equiv \ln K$ is modeled as a stationary, random field, whose autocorrelation function $\rho_Y \equiv \rho_Y(\mathbf{R})$ has an axisymmetric structure, i.e., $\mathbf{R} \equiv (\boldsymbol{x}_r, x_3/\lambda)/I$. The hydraulic head $H \equiv H(\boldsymbol{x})$ satisfies a stochastic Poisson equation

$$-\nabla^2 H(\boldsymbol{x}) = \nabla Y'(\boldsymbol{x}) \cdot \nabla H(\boldsymbol{x}) \tag{1}$$

where $Y' = \ln(K/K_G)$ is the fluctuation of the log-conductivity. The inner boundary conditions are those prevailing in the practice, i.e., constant heads at the boreholes, whereas the external boundary condition reads as: $\lim_{x\to\infty} |H(\boldsymbol{x})| < \infty$.

Central for quantifying transport are: (a) the mean, i.e., $\langle \boldsymbol{u} \rangle \equiv \langle \boldsymbol{u}(\boldsymbol{x}) \rangle$, of the (Darcy) velocity $\boldsymbol{u}(\boldsymbol{x}) = -(K/n)\nabla H(\boldsymbol{x})$ (being n the porosity, regarded herein as a given constant) and (b) the two-point velocity covariance, i.e., $u_{mn}(\boldsymbol{x}, \boldsymbol{y}) = \langle u_m^{(1)}(\boldsymbol{x})\, u_n^{(1)}(\boldsymbol{y}) \rangle$. In particular, the computation of the latter is not straightforward, owing to the complex dependence of the fluctuation $\boldsymbol{u}^{(1)} = \boldsymbol{u} - \langle \boldsymbol{u} \rangle$ upon the flow configuration.

2.1. Transport

Our approach follows the one developed by Cvetkovic and Dagan (1994) for transport in mean uniform flows, and subsequently adapted to radial-type flows (Dagan & Indelman, 1999; Severino et al., 2012). In line with these studies, pore-scale dispersion is neglected. In fact, it is known from experimental studies (see, e.g., Fernández-Garcia et al., 2004) pertaining to transport in radial flow configurations that pore-scale dispersion has a negligible impact on dispersion as compared to advection for the large Peclet numbers encountered in hydrological applications (Severino et al., 2011, 2012). In contrast, local dispersion plays an essential role in dilution, and it affects the concentration variance (Bellin et al., 2011; Fiori & Dagan, 2000). This study is limited, however, to investigating the BTCs as well as its moments, and therefore we shall neglect the effects of pore-scale dispersion.

1. *Eulerian picture*: For simplicity, we consider transport of two species, the liquid concentration (dissolved mass per liquid volume) $C \equiv C(\boldsymbol{x}, t)$ and the sorbed one (sorbed mass per liquid volume) $N \equiv N(\boldsymbol{x}, t)$. For these two species, advective transport is modeled by

$$\frac{\partial}{\partial t}(C + N) + \boldsymbol{u} \cdot \nabla C = 0 \tag{2}$$

The transport Equation 2 is supplemented with another function which mimics physical/chemical interaction between C and N. Equation 2 is solved for a medium which is initially solute free, and it is fed at $\boldsymbol{x}_0$ with a given concentration $C_0 \equiv C_0(t)$, i.e.,

$$C(\boldsymbol{x}, 0) = N(\boldsymbol{x}, 0) = 0, \qquad C(\boldsymbol{x}_0, t) = C_0(t) \tag{3}$$

Our aim is the computation of the BTC as function of the formation's parameters as well as reaction coefficients. Toward this aim, it is advantageous to cast the above transport problem within a Lagrangian framework.

2. *Lagrangian picture*: Assume that, for $t = 0$, a solute (either passive or reactive) is injected, and let $\boldsymbol{X}(t; \boldsymbol{x}_0) \equiv (X_1, X_2, X_3)$ be its trajectory, which satisfies the first-order equation

$$\frac{\mathrm{d}}{\mathrm{d}t}\boldsymbol{X} = \boldsymbol{u}(\boldsymbol{X}), \qquad \boldsymbol{X}(0; \boldsymbol{x}_0) = \boldsymbol{x}_0 \equiv (r_w, \theta, x_3) \tag{4}$$

In order to write Equation 2 within a Lagrangian framework, we replace the position $\boldsymbol{x} \equiv (x_1, x_2, x_3)$ with $\boldsymbol{\xi} \equiv (\xi_1, \xi_2, \xi_3)$, the latter being defined as

$$\xi_1 = \tau(x_1; \boldsymbol{x}_0), \qquad \xi_2 = x_2 - \eta(x_1; \boldsymbol{x}_0), \qquad \xi_3 = x_3 - \zeta(x_1; \boldsymbol{x}_0) \tag{5}$$

In Equation 5, τ is the travel time of a fluid particle released at the injecting well, and reaching a control plane (CP) placed perpendicularly to the horizontal segment connecting the two wells. Coordinates $\eta(x_1; \boldsymbol{x}_0) = X_2(\tau; \boldsymbol{x}_0)$ and $\zeta(x_1; \boldsymbol{x}_0) = X_3(\tau; \boldsymbol{x}_0)$ are such to determine the intersection on the CP at $t = \tau$ of the streamline originating at the injecting well (Figure 1). The relationship of the Lagrangian coordinates (τ, η, ζ) with the velocity field is determined by adapting to the present flow field the procedure of Cvetkovic and Dagan (1994), which was developed for mean uniform flows. By skipping the straightforward algebraic derivations (Equation 16 in Severino et al. (2005)), the final result is

$$\tau = \int_{-\bar{\ell}}^{x_1} \frac{\mathrm{d}s}{u_1(s)}, \qquad \eta = \int_{-\bar{\ell}}^{x_1} \mathrm{d}s\, \frac{u_2(s)}{u_1(s)}, \qquad \zeta = \int_{-\bar{\ell}}^{x_1} \mathrm{d}s\, \frac{u_3(s)}{u_1(s)}, \qquad x_1 \in \left]-\bar{\ell}, \bar{\ell}\right[\tag{6}$$

(hereafter we deal with $\bar{\ell} \equiv \ell/2$). It is seen from Equation 6 that the pair $(\eta, \zeta) \in$ CP depends upon the velocity field, solely (irrespective of τ). By employing the chain-rule of derivation (details can be found in Severino et al. (2005, Equation 17)), the transport Equation 2 is rewritten in terms of the $\boldsymbol{\xi} \equiv (\xi_1, \xi_2, \xi_3)$-coordinate Equation 5 as follows:

$$\frac{\partial}{\partial t}(C + N) + \frac{u_1(\boldsymbol{x})}{u_1(\boldsymbol{\xi})}\frac{\partial C}{\partial \xi_1} + \left[u_m(\boldsymbol{x}) - u_m(\boldsymbol{\xi})\frac{u_1(\boldsymbol{x})}{u_1(\boldsymbol{\xi})}\right]\frac{\partial C}{\partial \xi_m} = 0 \tag{7}$$

where Einstein's summation-convention over $m = 2, 3$ has been employed. Hence, taking $\xi_1 = \tau$ and $\xi_2 = \xi_3 = 0$, on the CP it results $\boldsymbol{x} \equiv \boldsymbol{\xi}$, and concurrently the transport Equation 7 becomes

$$\frac{\partial}{\partial t}(C+N)+\frac{\partial}{\partial \tau}C=0 \tag{8}$$

The Lagrangian concentrations C–N (for simplicity, we have maintained the same notation as in Equation 2) are function of t and τ solely, being the original three-dimensional nature of the problem now encapsulated in that of the travel time τ (see, also Dagan & Indelman, 1999; Severino et al., 2012). The solution $C \equiv C(\tau, t)$ of Equation 8 for a given set of initial/boundary conditions, is the same as that of one-dimensional transport advected by a unit velocity, and it shall be denoted hereafter as $\gamma \equiv \gamma(\tau, t)$. This latter can be determined for a large variety of reactions. In the sequel, we shall consider a fairly general linear nonequilibrium model, i.e.,

$$\frac{1}{\kappa}\frac{\partial}{\partial t}N = K_d\, C - N \tag{9}$$

being $\kappa\ \left(\mathrm{T}^{-1}\right)$ and $K_d\ (-)$ the desorption rate and the linear equilibrium partitioning coefficient, respectively. It is worth noting that the reaction Equation 9 contains the case of linear equilibrium model, i.e., $N = K_d\, C$, in the limit $\kappa \to \infty$. This is always true, except for a tiny (boundary layer) region where $\kappa^{-1}\frac{\partial}{\partial t}N \sim \mathcal{O}(1)$ (Severino et al., 2006).

2.2. BTC at Any CP Between the Two Wells

We aim at computing the mean flux concentration at any distance x_1 laying between the injecting/pumping wells (Figure 1). Thus, we consider a plume generated by injection of solute and reaching the CP at x_1. The element $\mathrm{d}\mathcal{F}$ of solute flux through a small surface $\mathrm{d}\boldsymbol{\sigma}$ belonging to the CP is given by $\mathrm{d}\mathcal{F} = n\,\mathrm{d}\boldsymbol{\sigma}\, u_1(\boldsymbol{\sigma})\gamma(\tau, t) = n\,\mathrm{d}\boldsymbol{\sigma}_0\, u_r\,(\boldsymbol{\sigma}_0)\,\gamma(\tau, t)$ (where the last equality stems from the continuity equation). As a consequence, the total solute flux $\mathcal{F} \equiv \mathcal{F}\,(t; x_1)$ through the CP is computed by means of convolution as

$$\mathcal{F}\,(t; x_1) = n\int_\Sigma\int_0^t \mathrm{d}\boldsymbol{\sigma}_0\,\mathrm{d}\bar{t}\, C_0\left(\bar{t}\right) u_r\,(\boldsymbol{\sigma}_0)\ \gamma\left(\tau, t-\bar{t}\right) \tag{10}$$

where Σ denotes the envelope of the injecting well. It is worth noting that $\mathcal{F}$ is clearly a function of the position x_1 due to the dependence of τ upon it (see the first of Equation 6). It represents the concentration in the fluid that is extracted (after complete mixing) over a large area of the CP. A similar token is applied to compute the fluid flux Q_f, the final result being $Q_f = n\int_\Sigma \mathrm{d}\boldsymbol{\sigma}_0\, u_r(\boldsymbol{\sigma}_0)$. Due to the random nature of u_r and γ, both $\mathcal{F}$ and Q_f are random fields, and we are interested in the computation of their spatial averages $\tilde{\mathcal{F}}$ and $\tilde{Q}_f$. Under ergodic conditions, that are assumed to apply (details upon such a requirement can be found in Dagan and Indelman (1999)), spatial averages are replaced by their ensemble counterparts, i.e.,

$$\tilde{\mathcal{F}}\,(t; x_1) \simeq \langle \mathcal{F}\,(t; x_1)\rangle = n\int_\Sigma\int_0^t \mathrm{d}\boldsymbol{\sigma}_0\,\mathrm{d}\bar{t}\, C_0\left(\bar{t}\right)\left\langle u_r\,(\boldsymbol{\sigma}_0)\ \gamma\left(\tau, t-\bar{t}\right)\right\rangle, \quad \tilde{Q}_f \simeq \langle Q_f\rangle \tag{11}$$

The ensemble average $\langle u_r\gamma\rangle$ has been computed into a general manner by Severino et al. (2012) (see Equations 12–14), and we limit in the sequel to quote the final result:

$$\langle u_r\,(\boldsymbol{\sigma}_0)\,\gamma(\tau, t)\rangle = \langle u_r\rangle\int_0^\infty \mathrm{d}\tau\, g\,(\tau, \boldsymbol{\sigma}_0)\ \gamma\,(\tau, t) \tag{12}$$

where $g \equiv g(\tau, \boldsymbol{\sigma}_0)$ is the probability density function (PDF) of the travel time of a fluid particle released at the injecting well and reaching the CP at $t = \tau$. Into deriving Equation 12, it is assumed that the velocity u_r along the injecting well is a stationary, random field (which implies that $\langle Q_f\rangle = n\langle u_r\rangle\Sigma$). Hence, the BTC $\tilde{C}^f \equiv \tilde{\mathcal{F}}/\tilde{Q}_f$ writes as

$$\begin{aligned}\tilde{C}^f\,(t; x_1) &\simeq \frac{1}{\Sigma}\int_\Sigma\int_0^\infty\int_0^t \mathrm{d}\boldsymbol{\sigma}_0\,\mathrm{d}\tau\,\mathrm{d}\bar{t}\, C_0\left(\bar{t}\right)\ \gamma\left(\tau, t-\bar{t}\right) g\,(\tau, \boldsymbol{\sigma}_0)\\ &= \fint_0^\pi\int_0^\infty \mathrm{d}\theta\,\mathrm{d}\tau\, g\,(\tau, \theta; x_1)\int_0^t \mathrm{d}\bar{t}\, C_0\left(\bar{t}\right)\ \gamma\left(\tau, t-\bar{t}\right), \qquad \fint \equiv \frac{1}{\pi}\int\end{aligned} \tag{13}$$

where switching from $\boldsymbol{\sigma}_0$ to θ is achieved by noting that, for $x_1 = -\bar{\ell}$, θ is the angle of attack of the streamline intersecting the CP at x_1. Thus, the BTC (Equation 13) is expressed via multiple quadratures whose physical interpretation is straightforward: it is the outcome of ensemble averaging along noninteracting stream tubes pertaining to those fluid particles which have reached (for fixed t) the CP. Due to the neglect of pore-scale dispersion, within each stream tube the dispersion mechanism is addressed only to the chemical nature of the solute, whereas the BTC is influenced by the stochastic variability of the velocity. Since the characteristic scale of this latter mechanism is the prevailing one, it is clear that most of the dispersion detected in the BTC (e.g., early tailing, etc.) is addressed to the heterogeneity of the porous formation. The computation of g is a formidable task, and some simplifying assumptions will be adopted in the sequel in order to achieve simple (i.e., analytical) results.

3. Approximate Solution to the Flow Field and Statistics of the Travel Time

The general problem stated so far is very hard to solve. As already mentioned, the difficulty is mainly due to the strong coupling between the spatially variable log-conductivity and the nonuniformity of the flow field. A relatively simple solution for the flow field can be achieved by adopting some approximations, which nevertheless keep the main features of the problem at stake. These assumptions, that were already employed in the past to solve similar problems (see e.g., Dagan & Indelman, 1999; Indelman et al., 2006; Severino, 2022), are briefly exploited in the sequel.

3.1. Simplifying Assumptions

1. The flow domain is large enough so that it can be regarded as unbounded, and concurrently ergodicity can be invoked. Generally, ergodicity is met when the aquifer's thickness D is much larger than the vertical integral scale I_v (Zech et al., 2018). Since $D \sim \mathcal{O}(10\,\mathrm{m})$ and $I_v \sim \mathcal{O}(10\,\mathrm{cm})$ (see, e.g., Tables 2.1 and 2.2 in Rubin, 2003), it is seen that ergodicity applies to the majority of the real settings.
2. We adopt a first-order approximation in the fluctuation Y', that is we deal with a weakly heterogeneous formation (Dagan & Indelman, 1999). As a consequence, we can expand the head H and the velocity $\boldsymbol{u}$ in asymptotic series

$$H(\boldsymbol{x}) = \sum_n H^{(n)}(\boldsymbol{x}), \qquad \boldsymbol{u}(\boldsymbol{x}) = \sum_n \boldsymbol{u}^{(n)}(\boldsymbol{x}) \tag{14}$$

where $|\mathcal{A}^{(n)}| \sim \mathcal{O}(Y'^n)$. In particular, the leading order terms $H^{(0)}$ and $\boldsymbol{u}^{(0)}$ pertain to the solution for a homogeneous medium of conductivity K_G.
3. We focus on anisotropic formations ($\lambda < 1$). In this case, accurate solutions for transport can be obtained by considering the following approximation for the first order (i.e., fluctuation) of the velocity

$$\boldsymbol{u}^{(1)}(\boldsymbol{x}) \simeq -Y'(\boldsymbol{x})\frac{K_G}{n}\nabla H^{(0)}(\boldsymbol{x}) \simeq Y'(\boldsymbol{x})\boldsymbol{u}^{(0)}(\boldsymbol{x}) \tag{15}$$

(Indelman & Dagan, 1999). It is emphasized that, in the limit $\lambda \to 0$ (stratified formation), Equation 15 becomes an exact first-order result. The approximation (Equation 15) was found to yield accurate results for transport already when $\lambda \le 0.2$ (Dagan & Indelman, 1999). Since sedimentary formations are as a rule anisotropic, such an approximation is relevant for the applications.
4. Injecting and pumping wells are replaced by a system of source and sink. This is valid for $r_w \ll \ell$. Since $r_w \sim \mathcal{O}(10 \div 50\,\mathrm{cm})$ whereas $\ell \sim \mathcal{O}(10 \div 50\,\mathrm{m})$, it results a reasonable approximation for most of the real cases. Thus, at the leading order the longitudinal velocity u_1 is

$$u_1^{(0)}(\phi,\theta) = \frac{Q_w}{2\pi n}\,\mathrm{Re}\left\{\frac{\mathrm{d}}{\mathrm{d}f}\left[\frac{\exp(f)-1}{\exp(f)+1}\right]\right\} = \frac{Q_w}{2\pi n\bar{\ell}}(1+\cos\theta\cosh\phi) \tag{16}$$

(Dagan & Indelman, 1999), where $f = \phi + \jmath(\theta - \pi)$ is the complex velocity potential (Bruggeman, 1999). Likewise, the horizontal coordinate $\boldsymbol{x}_r \equiv (x_1, x_2)$ writes as

$$\frac{x_1}{\bar{\ell}} \equiv \mathrm{Re}\left[\frac{\exp(f)+1}{\exp(f)-1}\right] = \frac{\sinh\phi}{\cosh\phi+\cos\theta}, \quad \frac{x_2}{\bar{\ell}} \equiv \mathrm{Im}\left[\frac{\exp(f)+1}{\exp(f)-1}\right] = \frac{\sin\theta}{\cosh\phi+\cos\theta} \tag{17}$$

with $\phi \in \mathbb{R}$ and $\theta \in [0, \pi[$. Note that, in the (ϕ, θ)-framework, the locations of the source and the sink correspond to $\phi \to -\infty$ and to $\phi \to +\infty$, respectively.

3.2. Travel Time Statistics

The travel time τ is obtained from the first of Equation 6, and therefore it is determined by the curvilinear coordinate s along a random streamline originating at the source and reaching the CP with velocity u_1 (Figure 1). As a consequence, τ is also a random field, and we aim at computing its first-order and second-order moment. Based on the above simplifying assumptions, up to the first-order we may write (see Equation 15)

$$\boldsymbol{u}(\boldsymbol{x}) \simeq \boldsymbol{u}^{(0)}(\boldsymbol{x}) + \boldsymbol{u}^{(1)}(\boldsymbol{x}) = \boldsymbol{u}^{(0)}(\boldsymbol{x}) \left[1 + Y'(\boldsymbol{x})\right] \tag{18}$$

Thus, switching to the variables (ϕ, θ, x_3) in the first of Equation 6 and accounting for Equation 18, one has

$$\tau(\phi_1, \theta, x_3) = \int_{-\infty}^{\phi_1} \frac{\mathrm{d}\omega \, (\mathrm{d}\bar{x}_1/\mathrm{d}\omega)}{u_1(\omega, \theta, x_3)} \simeq \int_{-\infty}^{\phi_1} \frac{\mathrm{d}\omega \, (\mathrm{d}\bar{x}_1/\mathrm{d}\omega)}{u_1^{(0)}(\omega, \theta)\left[1 + Y'(\omega, \theta, x_3)\right]} \tag{19}$$

being the pair (ϕ, θ) uniquely determined by Equation 17 for each $\boldsymbol{x}_r \equiv (x_1, x_2)$. In particular, the upper bound in the integrals (Equation 19) is $\phi_1 \to \ln\left[\left(\bar{\ell} + x_1\right) / \left(\bar{\ell} - x_1\right)\right]$. Then, by accounting for Equation 16, and computing the derivative $\mathrm{d}\bar{x}_1/\mathrm{d}\omega$ by means of the first of Equation 17, it yields

$$\tau(\phi_1, \theta, x_3) = 2\,\tau_c \int_{-\infty}^{\phi_1} \mathrm{d}\omega \, \frac{\left[1 + Y'(\omega, \theta, x_3)\right]^{-1}}{(\cosh\omega + \cos\theta)^2}, \qquad \tau_c = \frac{n\pi}{Q_w}\bar{\ell}^2 \tag{20}$$

The travel time needed to reach the source is obtained by taking the limit $\phi_1 \to +\infty$ into Equation 20 (which coincides with Equation 28 in Dagan and Indelman (1999)). In order to compute the first two moments of τ, we expand, in the spirit of the perturbation approximation discussed in (ii), the term $(1 + Y')^{-1}$, thus obtaining

$$\tau^{(0)}(\phi_1, \theta) = 2\,\tau_c \int_{-\infty}^{\phi_1} \frac{\mathrm{d}\omega}{(\cosh\omega + \cos\theta)^2}, \quad \tau^{(1)}(\phi_1, \theta, x_3) = -2\,\tau_c \int_{-\infty}^{\phi_1} \frac{\mathrm{d}\omega \, Y'(\omega, \theta, x_3)}{(\cosh\omega + \cos\theta)^2} \tag{21}$$

At the zero-order, the mean travel time is the leading order term, i.e., $\langle\tau\rangle \simeq \tau^{(0)}(\phi_1, \theta)$, and it is derived analytically (by converting the hyperbolic function into its exponential form, and employing integration by substitution) as follows:

$$\begin{aligned}
\langle\tau(\phi_1, \theta)\rangle &= 2\,\tau_c \int_{-\infty}^{\phi_1} \frac{\mathrm{d}\omega}{(\cosh\omega + \cos\theta)^2} = 8\tau_c \int_{-\infty}^{\phi_1} \frac{\exp\omega \, \mathrm{d}(\exp\omega)}{(\exp 2\omega + 2\exp\omega\cos\theta + 1)^2} \\
&= 8\tau_c \int_0^{\exp\phi_1} \frac{t\,\mathrm{d}t}{(t^2 + 2t\cos\theta + 1)^2} = -4\tau_c \frac{\partial}{\partial b} \int_0^{\exp\phi_1} \frac{\mathrm{d}t}{t^2 + 2\,b\,t + 1}\bigg|_{b \equiv \cos\theta} \\
&= \frac{2\,\tau_c}{\sin^2\theta}\left\{\frac{\cos\theta + \exp\phi_1}{\cos\theta + \cosh\phi_1} - 2\frac{\cos\theta}{\sin\theta}\left[\arctan\left(\frac{\cos\theta + \exp\phi_1}{\sin\theta}\right) - \arctan\left(\frac{\cos\theta}{\sin\theta}\right)\right]\right\}
\end{aligned} \tag{22}$$

whereas the variance $\sigma_\tau^2(\phi_1, \theta) \equiv \left\langle\left[\tau^{(1)}(\phi_1, \theta, x_3)\right]^2\right\rangle$ reads as

$$\sigma_\tau^2(\phi_1, \theta) = 4(\tau_c\,\sigma_Y)^2 \int_{-\infty}^{\phi_1}\int_{-\infty}^{\phi_1} \frac{\mathrm{d}\omega' \, \mathrm{d}\omega'' \, \rho_Y\left[\boldsymbol{x}_r(\omega', \theta) - \boldsymbol{x}_r(\omega'', \theta)\right]}{\left[(\cosh\omega' + \cos\theta)(\cosh\omega'' + \cos\theta)\right]^2} \tag{23}$$

As it will be clearer later on, the cross-variance $\sigma_{Y\tau}$ is also required to solve transport. It is obtained by averaging $\tau^{(1)}$ multiplied by Y', the final result being

$$\sigma_{Y\tau}(\phi_1, \theta) = -2\tau_c\sigma_Y^2 \int_{-\infty}^{\phi_1} \mathrm{d}\omega \, \frac{\rho_Y\left[\boldsymbol{x}_r(\phi_1, \theta) - \boldsymbol{x}_r(\omega, \theta)\right]}{(\cosh\omega + \cos\theta)^2} \tag{24}$$

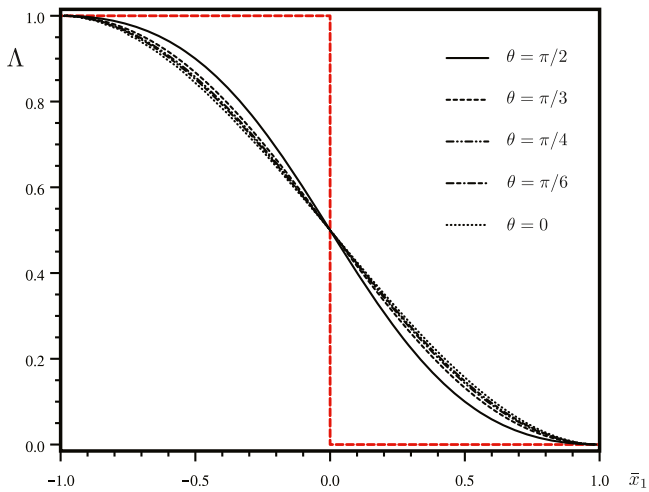

Figure 2. Dependence of the Λ-function (Equation 27) upon the scaled distance $\bar{x}_1 \equiv x_1/\bar{\ell}$, and several values of the attack-angle θ. The red, dashed, thick line corresponds to $\theta \to \pi^-$.

Unlike the fluctuation $\tau^{(1)}$ (which has a three-dimensional structure), the (cross)-variances (Equations 23 and 24) depend only upon the coordinates (ϕ, θ). This is due to the fact that, at the leading order, the flow field does not depend upon x_3. By taking $\phi_1 \to +\infty$ in Equation 22, it yields

$$\langle \tau(\infty, \theta) \rangle = 4\,\tau_c\,\frac{1 - \theta\cot\theta}{\sin^2\theta} \tag{25}$$

in agreement with Koplik et al. (1994). The mean travel time (Equation 22), together with Equation 25, allows to write \beginAlign

$$\langle \tau(\phi_1, \theta) \rangle = \langle \tau(\infty, \theta) \rangle \left[1 - \Lambda(\phi_1, \theta)\right] \tag{26}$$

$$\Lambda(\phi, \theta) = \frac{1}{1 - \theta\cot\theta}\left\{1 - \frac{\cos\theta + \exp\phi}{2\,(\cos\theta + \cosh\phi)} - \frac{\cos\theta}{\sin\theta}\left[\frac{\pi}{2} - \arctan\left(\frac{\cos\theta + \exp\phi}{\sin\theta}\right)\right]\right\} \tag{27}$$

The representation (Equations 26 and 27) enables one to regard the mean travel time $\langle\tau\rangle$ as product between $\langle \tau(\infty, \theta) \rangle$ (accounting for the mean travel time from the sink, i.e., $\phi \to -\infty$, to the source, i.e., $\phi \to +\infty$) and a function $1 - \Lambda$, which adjusts $\langle\tau(\infty, \theta)\rangle$ in order to provide the mean travel time at any CP. It is seen that the following bounds $0 = \Lambda(+\infty, \theta) \le \Lambda(\phi_1, \theta) \le \Lambda(-\infty, \theta) = 1$ hold. In Figure 2, we have depicted Λ as function of the dimensionless distance $\bar{x}_1 \equiv x_1/\bar{\ell} = (\exp\phi_1 - 1)\,/\,(\exp\phi_1 + 1) \in [-1, +1]$, for several values of the attack-angle θ. It is seen that the various Λ-functions slightly differ with θ (a similar behavior was highlighted by Indelman et al. (2006), although in a different flow configuration). For $\theta \to \pi^-$ (red dashed line), one has $\Lambda \to h(\pi - \theta)$, being h the Heaviside step function defined as: $h(x) = 1$ for $x > 0$, $h(0) = 1/2$, and $h(x) = 0$ for $x < 0$. As a consequence, $\theta \to \pi^-$ corresponds to $\langle\tau\rangle = 0$ (stagnation point). By noting that

$$\frac{\pi}{2} - \arctan\left(\frac{1 + \cos\theta}{\sin\theta}\right) = \arctan\left(\frac{\sin\theta}{1 + \cos\theta}\right) = \arctan\left(\tan\frac{\theta}{2}\right) = \frac{\theta}{2}, \quad \forall\theta \in [0, \pi[\tag{28}$$

and accounting for Equation 27, it yields $\Lambda(0, \theta) = 1/2$ (Figure 2). In the relationships (Equation 28) we have made use of the identity $\pi/2 = \arctan x + \arctan(1/x)$ (valid for any $x > 0$), and employed the parametric representation of circular functions. Hence, the mean travel time required to cover the distance from the sink $\left(x_1 = -\bar{\ell}\right)$ to $x_1 = 0$ is the half of $\langle\tau(\infty, \theta)\rangle$, irrespective of the trajectory (any θ). From a mechanical point of view, this is explained by noting that: (a) the distance from the source $\left(x_1 = -\bar{\ell}\right)$ to $x_1 = 0$ (corresponding to $\phi = 0$) is the half of that between the system of source/sink, and that (b) the flow is steady. To discuss the behavior of Λ with the different attack-angles, we remind that $u_1 \sim 1 + \cos\theta\cosh\phi_1$ (see Equation 16), and therefore the mean travel time $\tau^{(0)}$ (which goes like u_1^{-1}) is larger for the lowest $\cos\theta$ when $\phi_1 < 0$, and vice versa. Note that the above results are easily extended to the σ_Y^2 -order approximation of the mean travel time $\langle\tau\rangle = \tau^{(0)} + \langle\tau^{(2)}\rangle$. In fact, from Equation 20, one has $\tau^{(2)}(\phi_1, \theta, x_3) = 2\,\tau_c \int_{-\infty}^{\phi_1} \frac{\mathrm{d}\omega\, Y'^2(\omega, \theta, x_3)}{(\cosh\omega + \cos\theta)^2}$, and concurrently the previous discussion is valid even at the σ_Y^2-order, provided that one replaces $\tau^{(0)} \to \left(1 + \sigma_Y^2\right)\tau^{(0)}$ (where we have made use of the stationarity of Y).

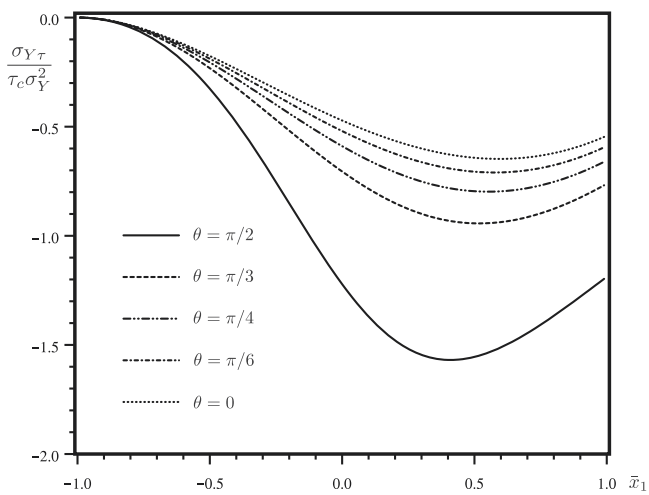

Figure 3. Dependence of the cross-variance $\sigma_{Y\tau} \equiv \sigma_{Y\tau}(\theta, \phi)$ relative to $\tau_c\sigma_Y^2$ upon the dimensionless distance $\bar{x}_1 \equiv x_1/\bar{\ell}$, and several values of the attack-angle $\theta\left(\bar{\ell} = I\right)$. Curves refer to the exponential model of ρ_Y.

The cross-variance $\sigma_{Y\tau}$ is always negative (Figure 3), since an increase in Y' corresponds to an increase in the velocity's fluctuation (Equation 15), and concurrently to a reduction of τ. The cross-variance $\sigma_{Y\tau}$ is evaluated for $\bar{\ell} = I$, and by carrying out numerically the single quadrature in Equation 24. In particular, this has been done by adopting exponential model for the auto-correlation (the same insights are drawn by dealing with a Gaussian ρ_Y as well as the power law, provided that the anisotropy ratio is much lesser than

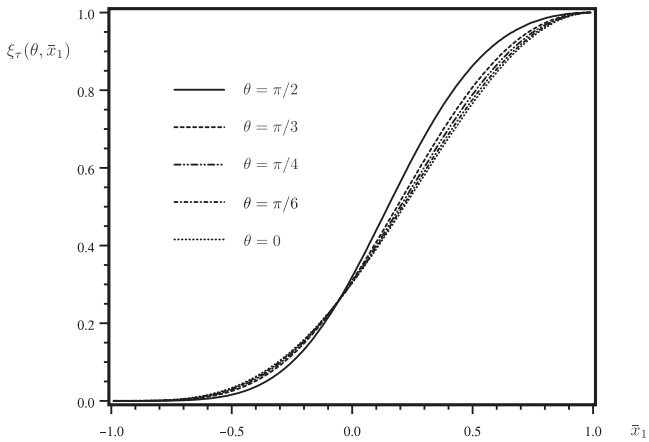

Figure 4. Dependence of $\xi_\tau \equiv \xi_\tau(\theta, \bar{x}_1)$ upon $\bar{x}_1$, and several values of the attack-angle θ. Other parameters are the same of Figure 3.

one). A closed form is obtained for $\theta = 0$ (i.e., along the central stream line), for which in Equation 24 one has

$$\rho_Y \equiv \exp|x_1(\phi_1, 0) - x_1(\omega, 0)|, \qquad x_1(a, 0) = \frac{\sinh a}{\cosh a + 1} = \frac{\exp a - 1}{\exp a + 1} \tag{29}$$

By omitting the algebraic derivations (that are very similar to those which have led to Equation 22), the final result reads as follows:

$$\sigma_{Y\tau}(\bar{x}_1) = -\tau_c \sigma_Y^2 \bar{I}\left[1 - \bar{I}^2 - \left(\bar{x}_1 - \bar{I}\right)^2 + 2\bar{I}\left(1 + \bar{I}\right)\exp\left(-\frac{1 + \bar{x}_1}{\bar{I}}\right)\right], \quad \bar{I} \equiv \frac{I}{\bar{\ell}} \tag{30}$$

To illustrate the dependence of the variance (Equation 23) upon the position of the CP, in Figure 4, we have depicted the ratio $\xi_\tau(\theta, \bar{x}_1) = \sigma_\tau^2(\theta, \bar{x}_1)/\sigma_\tau^2(\theta, 1)$ between the variance (Equation 23) and its value at the sink ($\bar{x}_1 = 1$) as function of $\bar{x}_1 \equiv x_1/\bar{\ell}$, and a few values of the attack-angle θ. It is seen that the variance σ_τ^2 at any x_1 is always lesser that its asymptotic. This is understandable in view of the fact that, in order to reach the sink, any fluid particle covers the longest pathway (irrespective of θ), therefore increasing its travel time (and concurrently the variance). Likewise the case of the cross-variance (30), for the central streamline, an analytical solution can be derived by dealing with the exponential model of the autocorrelation. The final result reads as $\sigma_\tau^2(\bar{x}_1) = 8(\tau_c \sigma_Y)^2 \bar{I}\,\bar{\sigma}_\tau^2(\bar{x}_1)$, being the scaled variance $\bar{\sigma}_\tau^2$ given by

$$\begin{aligned}\bar{\sigma}_\tau^2(\alpha) \;=\; & \bar{I}^3\left(1 - \bar{I}^2\right) + \frac{\bar{I}^2}{6}\left(\alpha^3 - 3\alpha - 2\right) - \frac{\bar{I}}{8}\left(1 - \alpha^2\right)^2 + \frac{1}{60}\left(3\alpha^2 - 9\alpha + 8\right)(1 + \alpha)^3 + \\ & \bar{I}^2\left(1 + \bar{I}\right)\left[\bar{I}\left(\bar{I} + \alpha\right) - \frac{1}{2}\left(1 - \alpha^2\right)\right]\exp\left(-\frac{1 + \alpha}{\bar{I}}\right)\end{aligned} \tag{31}$$

Now, we wish to discuss two asymptotics. The first one corresponds to $\bar{\ell} \ll I$ (near field). In this case, flow can be investigated by taking $\rho_Y \simeq 1$. Thus, substitution of the latter into (Equation 23) leads to $\sigma_\tau^2 = (\sigma_Y \langle\tau\rangle)^2$. As a consequence, the ratio ξ_τ behaves like $(1 - \Lambda)^2$, with the Λ-function given by Equation 27. The other extreme of $\bar{\ell} \gg I$ (far field) refers to a flow that behaves like a mean uniform one (see discussion in Severino (2011)). In this case, the variance (Equation 23) is studied straightforwardly by considering that, for fixed $\bar{\ell}$, the condition $\bar{\ell} \gg I$ corresponds to $I \to 0$, and concurrently in the expression (Equation 23) one can replace the autocorrelation of Y with a white noise signal (i.e., $\rho_Y \equiv \delta$). By skipping the cumbersome algebraic derivations, one has

$$\sigma_\tau^2(x_1, \theta) = 16\frac{(\tau_c \sigma_Y)^2}{\sin^4\theta}\bar{I}\left[\Upsilon\left(\frac{\bar{\ell} + x_1}{\bar{\ell} - x_1}, \cos\theta\right) - \Upsilon(0, \cos\theta)\right] \tag{32}$$

where we have set

$$\begin{aligned}\Upsilon(u, b) = & \frac{b}{\sqrt{1 - b^2}}\left[\frac{|b|}{4}\ln\left|\frac{u - \beta^+}{u - \beta^-}\right| - \arctan\left(\frac{u + b}{\sqrt{1 - b^2}}\right)\right] \\ & - \frac{bu + 1}{2\left(u^2 + 2bu + 1\right)}, \quad (|b| < 1)\end{aligned} \tag{33}$$

with $\beta^\pm = -1/b \pm \sqrt{1/b^2 - 1}$. To compute the BTC (Equation 13), the PDF of a fluid particle released at the pumping well and reaching the CP at $t = \tau$ is required. At the σ_Y^2-order, it is given by

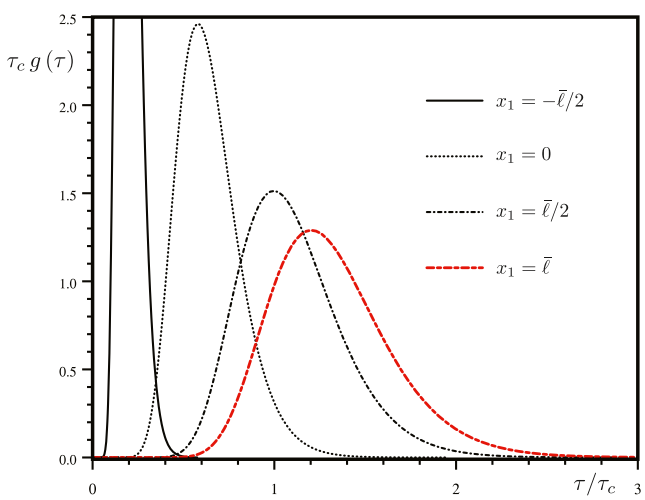

Figure 5. Scaled probability density function (PDF) (Equation 34) of the travel time of a fluid particle released at the injecting well with an attack-angle equal to $\theta = 0$, and reaching a control plane (CP) at $x_1 = -\bar{\ell}/2;\ 0;\ \bar{\ell}/2$. Other parameters: $\sigma_Y^2 = 0.1$ and $I = \bar{\ell}$. The PDF at the recovery well (i.e., $x_1 = \bar{\ell}$) is also depicted (thick red dashed line).

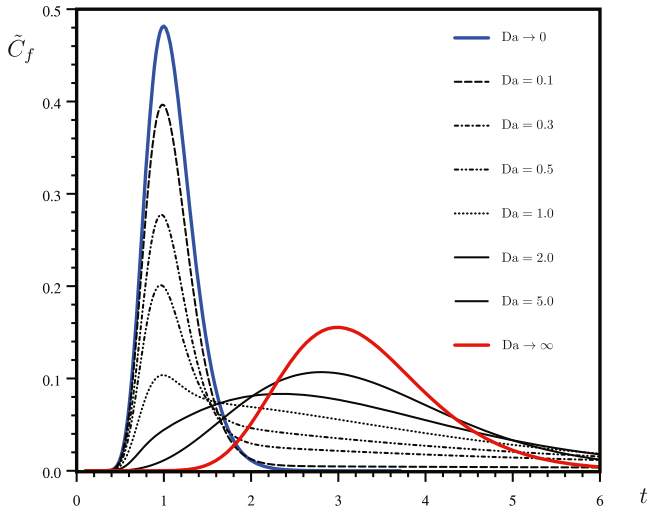

Figure 6. Normalized breakthrough curve (BTC) (Equation 37) versus the scaled time t, and several values of the Damköhler number Da. Other parameters: $\sigma_Y^2 = 0.1$, $I = \bar{\ell}$, $x_1 = \bar{\ell}/2$, and $K_d = 2$.

$$g(\tau,\theta;x_1) = \frac{\langle\tau\rangle/\tau}{\sqrt{2\pi}\,\sigma_\tau}\left[1+\langle\tau\rangle\frac{\sigma_{Y\tau}}{\sigma_\tau^2}\ln\left(\frac{\tau}{\langle\tau\rangle}\right)\right] \exp\left\{-\frac{1}{2}\left[\frac{\langle\tau\rangle}{\sigma_\tau}\ln\left(\frac{\tau}{\langle\tau\rangle}\right)\right]^2\right\} \tag{34}$$

(for details, see Appendix B in Dagan and Indelman (1999)), with $\langle\tau\rangle$, σ_τ^2, and $\sigma_{Y\tau}$, due to their dependence upon the position of the CP, given by Equations 22–24. In Figure 5, we have depicted the scaled (multiplied by τ_c) PDF (Equation 34) as function of the nondimensional travel time τ/τ_c, for $\theta = 0$ and several values of x_1. Results are shown for exponential autocorrelation ρ_Y. For comparison purposes, we have also depicted (Equation 34) at the sink (red dashed line) corresponding to the PDF considered by Dagan and Indelman (1999). The most evident feature is that the higher is x_1 the larger is the dispersion. In fact, for increasing x_1 the portion of the domain which is sampled by fluid particles released at the source is larger, and concurrently the amount of sampled heterogeneity is increasing, ultimately causing an augmented dispersion.

4. Discussion

We now wish to assess the impact of the reaction parameters upon the shape of the BTC at any CP $x_1 \in]-\bar{\ell},\bar{\ell}[$, within a given formation. Toward this aim, we consider a pulse-like (i.e., $C_0 \equiv \delta$) injection of a specific (divided by the well's envelope and by the flux at the injecting well) solute mass m_0. In this case, Equation 13 writes as

$$\tilde{C}^f(t;x_1) = m_0 \fint_0^\pi \int_0^\infty \mathrm{d}\theta\,\mathrm{d}\tau\,\gamma(\tau,t)\,g(\tau,\theta;x_1) \tag{35}$$

(that generalizes the result of Severino et al. (2012)). The BTC (Equation 35) is sought as ensemble average over the attack-angle θ, which is reasonable to regard as a random variable uncorrelated with the travel time τ, and uniformly distributed within the interval $]0,\pi[$ (see also Zech et al., 2018). The characteristic function $\gamma \equiv \gamma(\tau,t)$ for the advective/reaction model (Equations 8 and 9) is

$$\gamma(\tau,t) = \exp(-\kappa K_d t)\,\delta(t-\tau) + K_d\kappa^2\tau\exp[-\kappa(K_d\tau+t-\tau)]\,\tilde{\mathrm{I}}_1\left[K_d\kappa^2\tau(t-\tau)\right]h(t-\tau) \tag{36}$$

(see, e.g., Severino & Indelman, 2004), where $\tilde{\mathrm{I}}_1(Z) \equiv \mathrm{I}_1(2\sqrt{Z})/\sqrt{Z}$ and I_n is the n-order modified Bessel function of the first kind. The function (Equation 36) results made up by: (a) a propagating pulse that decays exponentially with the time and (b) a continuous distribution determined by the reaction's parameters. Substitution of Equation 36 into Equation 35 and scaling the concentration and the time by m_0/τ_c and τ_c, respectively (although, for simplicity, we retain the same notations), lead to

$$\tilde{C}^f(t;x_1) = K_d\,\mathrm{Da}^2 \fint_0^\pi \int_0^t \mathrm{d}\theta\,\mathrm{d}\tau\,\tau\exp[-\mathrm{Da}(K_d\,\tau+t-\tau)]\,\tilde{\mathrm{I}}_1\left[K_d\,\mathrm{Da}^2\tau(t-\tau)\right]\,g(\tau,\theta;x_1) + \exp(-K_d\,\mathrm{Da}\,t)\,\tilde{C}_p(t;x_1) \tag{37}$$

where the Damköhler number $\mathrm{Da} \equiv \kappa\tau_c$ is the ratio between the characteristic flow time τ_c and the reaction time κ^{-1}. In addition, $\tilde{C}_p(t;x_1) \equiv \fint_0^\pi \mathrm{d}\theta\,g(t,\theta;x_1)$ represents the normalized BTC that one would recover if the injected solute were a passive one ($\mathrm{Da} \to 0$). The BTC in Equation 37 can be thought of as a superposition of two transport mechanisms. The first term represents the contribution along those trajectories of solute particles which, at time t, have not yet reached the CP (i.e., $\tau < t$). The second term in Equation 37 is the contribution of the streamlines along which solute particles have already reached the CP at the time t.

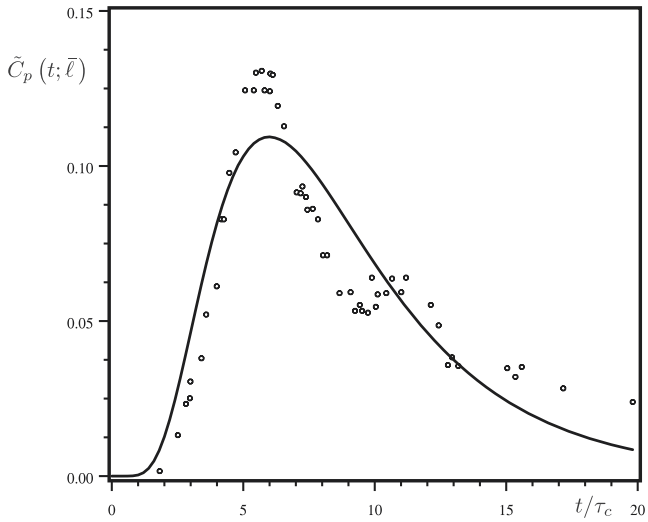

Figure 7. Comparison between experimental data (symbols) of the dipole tracer test at the Mobile's aquifer (Molz et al., 1986) and the analytical solution (line) $\tilde{C}_p \equiv \tilde{C}_p\left(t;\bar{\ell}\right)$, as function of the nondimensional time t/τ_c. Parameters: $\sigma_Y^2 = 0.24$ (measured) and $I = 3.8$ m (fitted).

In Figure 6, we have shown the BTC (Equation 37) versus t for some values of the Damköhler number, at $x_1 = \bar{\ell}/2$ ($K_d = 2$ and $\sigma_Y^2 = 0.1$). For a very slow reaction (Da $\to$ 0), the sorbed concentration N is completely blocked off, and the solute behaves like a conservative one. To the contrary, a very fast reaction (Da $\to \infty$) implies that the two concentrations mix instantaneously, and the BTC behaves as that obtained by dealing with a linear equilibrium model, i.e., $N = K_d C$. This is also confirmed by the fact that the center of gravity of red BTC (corresponding to that pertaining to the linear equilibrium model) is $R = 1 + K_d = 3$ times head that (blue line) attached to a passive scalar. At intermediate values of the Damköhler number Da, the BTC clearly exhibits a tail due to the delay caused by the ongoing mass transfer between the sorbed and liquid phase.

4.1. Application to Field Experiments

It is interesting to illustrate the theoretical model to real data. In particular, we consider a tracer transport in a dipole flow, and we wish to show how dispersion between the sink/source can be quantified once the BTC at the recovery well is monitored. Toward this aim, we deal with two experiments where the BTC, monitored at the sink, is used to calibrate the heterogeneity structure of the hosting formations (in close analogy to Zech et al. (2018)). Dispersion is quantified by means of the second-order temporal moment

$$\mathcal{T}_2(x_1) = \frac{\mathcal{M}_2(x_1)}{\mathcal{M}_0(x_1)} - \left[\frac{\mathcal{M}_1(x_1)}{\mathcal{M}_0(x_1)}\right]^2, \qquad \mathcal{M}_n(x_1) = \int_0^\infty \mathrm{d}t\, t^n \tilde{C}^f(t;x_1) \qquad (n \in \mathbb{N}) \tag{38}$$

where, due to the nature (passive) of the solute, the flux concentration $\tilde{C}^f$ coincides with Equation 34, and concurrently one has (we omit the derivations)

$$\mathcal{T}_2(x_1) = \int_0^\pi \mathrm{d}\theta \langle\tau\rangle^2 \left\{ \left(1 + 2\frac{\sigma_{Y\tau}}{\langle\tau\rangle}\right) \exp\left[2\left(\frac{\sigma_\tau}{\langle\tau\rangle}\right)^2\right] - \left(1 + \frac{\sigma_{Y\tau}}{\langle\tau\rangle}\right)^2 \exp\left[\left(\frac{\sigma_\tau}{\langle\tau\rangle}\right)^2\right] \right\} \tag{39}$$

being the mean $\langle\tau\rangle \equiv \langle\tau(x_1,\theta)\rangle$ and the two (cross)variances, i.e., $\sigma_\tau^2 \equiv \sigma_\tau^2(x_1,\theta)$ and $\sigma_{Y\tau} \equiv \sigma_{Y\tau}(x_1,\theta)$, given by Equations 22–24. Thus, unlike previous studies of Dagan and Indelman (1999) and Zech et al. (2018), our model also provides a simple expression to quantify dispersion in the strip $x_1 \in]-\bar{\ell},\bar{\ell}[$. The experiments are fully described in Molz et al. (1986) and Robson (1974). For the purposes of the present study, they are summarized in the sequel.

4.1.1. Experiment at the Mobile's Aquifer

The aquifer consists of interbedded sands and clays, as a result of subsequent depositions by the Mobile River. The formation is mildly heterogeneous $\left(\sigma_Y^2 = 0.24\right)$ with porosity n equal to 0.35. The aquifer's thickness is 21.6 m, and roughly located between 40-m and 60-m depth. Two fully penetrating wells ($2\ell = 38.3$ m) were used for the purposes of the tracer test, with a forcing volumetric flow rate $Q = 0.946$ m^3/min. A pulse-like of tracer (bromide), with concentration $C_0 = 169$ mg/ℓ, was injected (for 76.6 hr) at the source, and it was recovered at the sink over 32.5 days. The unknown horizontal integral scale I has been identified by a best fitting between the measured and the theoretical BTC at the sink. The matching lead to $\bar{I} \equiv 2I/\ell \simeq 0.4$ (and concurrently $I \simeq 3.8$ m). Thus, with σ_Y^2 taken from the measurements and $\bar{I}$ determined by a fitting, we have depicted (continuous line) the theoretical BTC (Equation 35) at the sink (Figure 7), along with the experimental data (symbols) from Molz et al. (1986).

4.1.2. Experiment at the Barstow's Aquifer

The aquifer, whose thickness is 27.45 m, exhibits a moderate degree of heterogeneity $\left(\sigma_Y^2 = 0.5\right)$ with porosity equal to 0.30. The doublet, working at $Q = 0.208$ m^3/min, was such that $2\ell = 6.4$ m. The tracer (chloride) was constantly injected for 84 hr, and it was recovered at the sink during the same period. As such, unlike the Mobile-experiment, here the recovered BTC is the cumulative distribution function, i.e.,

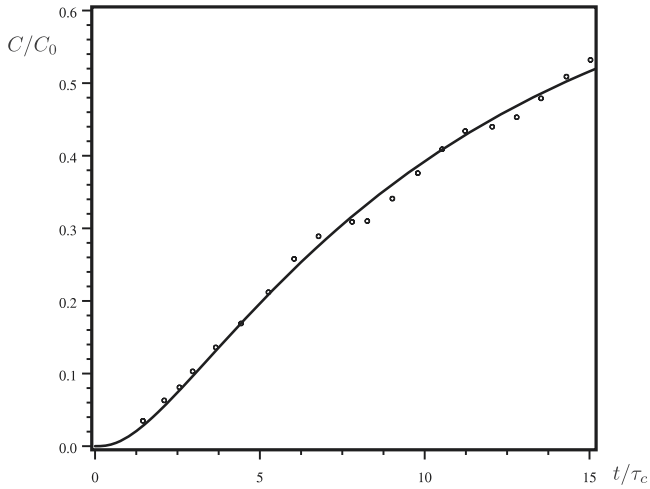

Figure 8. Comparison between experimental data (symbols) of the dipole tracer test at the Barstow's aquifer (Robson, 1974) and the analytical solution (Equation 40) evaluated at the pumping well ($\bar{x}_1 = 1$). Parameters: $\sigma_Y^2 = 0.50$ (measured) and $I = 1.9$ m (fitted).

$$\frac{C(t;x_1)}{C_0} = \oint_0^\pi \mathrm{d}\theta \int_0^t \mathrm{d}\tau\, g(\tau,\theta;x_1) = \frac{1}{2\pi} + \frac{1}{2} \oint_0^\pi \mathrm{d}\theta \left[\mathrm{erf}\left(\frac{\sqrt{2}}{2}\, a\right) - \sqrt{\frac{2}{\pi}}\, b \exp\left(-\frac{a^2}{2}\right)\right] \tag{40}$$

being $a \equiv (\langle\tau\rangle/\sigma_\tau)\ln(t/\langle\tau\rangle)$ and $b \equiv \sigma_{Y_t}/\sigma_\tau$. Owing to the lack of information about the geostatistics of Y, the horizontal integral scale has been identified, similarly to the previous case, i.e., by means of a best fitting procedure leading to $\bar{I} = 0.6$ ($I = 1.9$ m). In Figure 8, we have depicted the BTC at the sink, together with the experimental BTC from Robson (1974).

To conclude the analysis of the two experiments, it is worth noting that, although no information is available about the vertical integral scale I_v, this latter, being generally $\mathcal{O}(1\div10\,\mathrm{cm})$ (see Tables 2.1 and 2.2 in Rubin, 2003), is such that $\lambda \sim \mathcal{O}\left(10^{-2}\div10^{-1}\right)$, in reasonable agreement with the assumption (iii) underlying the present study. Now, we wish to discuss the dispersion mechanism that is expected to occur in the zone between the two wells in the experiments at stake. This can be done by evaluating the second-order moment (Equation 39). In particular, we focus on the central trajectory, since most of the dispersion takes place along it (Severino, 2022). In Figure 9, we have depicted the scaled (by τ_c^2) second-order moment $\mathcal{T}_2$ at both the Mobile (black line) and Barstow (blue) aquifer. Overall, $\mathcal{T}_2$ is monotonously increasing with the distance $\bar{x}_1 \in]-1,+1[$, therefore reaching the maximum at the recovery (pumping) well. From one side, this is due to the fact that the released solute experiences an increasing portion of the medium (and concurrently of heterogeneity), with increasing x_1. From the other, the advective velocity becomes unbounded at the sink, and therefore dispersion there increases. As expected, dispersion at the Barstow aquifer is larger (for fixed $\bar{x}_1$) than that at the Mobile aquifer due to the bigger (in practice two times) σ_Y^2 (and given the fact that the parameter $\bar{I}$ is almost the same for the two experiments).

While this example shows how the information acquired at the sink can be readily used to quantify the dispersion mechanism occurring in the intermediate zone between the two wells, there are other practical applications which may benefit from the theoretical results developed within the present study. (a) For example, one can select the proper strength Q_w and the distance ℓ of the doublet in order to design in situ remediation strategies (Severino, 2022). (b) The knowledge of the dispersion-pattern in the strip $]-\bar{\ell},+\bar{\ell}[$ is also crucial for the use of chemicals to neutralize dissolved pollutants (Di Dato et al., 2018). (c) Another possible application pertains the identification of the aquifer as well as reactive parameters by field tests, by means of an inverse procedure. This can be achieved by injecting two solutes, a conservative and a reactive one, in the recharging well. Subsequently, the different BTCs in the pumping well may be analyzed with the aid of the present solutions.

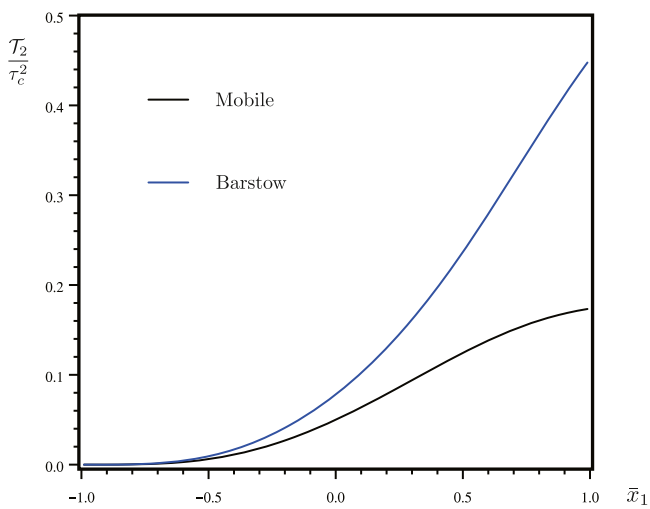

Figure 9. Dependence upon the dimensionless distance $\bar{x}_1 = x_1/\bar{\ell}$ of the nondimensional moment $\mathcal{T}_2/\tau_c^2$ quantifying the dispersion mechanism along the central trajectory between the injecting ($\bar{x}_1 = -1$) and at the pumping ($\bar{x}_1 = 1$) well in the transport experiments at the Mobile's (black line) and Barstow's (blue line) aquifer.

To conclude, we wish to discuss briefly whether one can use a homogeneous transport equation with fictitious advection-dispersion coefficients resembling the effects of the real (i.e., heterogeneous) setting. One way to achieve such an upscaling is dealing with effective dispersion/advection coefficients, defined as those that, in the transport equation, lead to the mean concentration. For transport in nonuniform mean flows (like the one considered in the present study), it is known that an effective dispersion coefficient cannot be defined in the above (i.e., classical) sense (Indelman & Dagan, 1999). Alternatively, one could define an equivalent dispersion coefficient such that the rate of change of the second-order spatial moment of the plume is equal to that observed in the heterogeneous formation. However, such an avenue is matter of debate for, at least, two reasons: (a) there is no experimental and/

or numerical proof of its feasibility and (b) it should depend only upon quantities which can be easily measured in the field (typically the hydraulic head and mobile concentration). Another possibility is to regard the effective dispersion coefficient like that which, in a coarse grid simulation, provides the same solution of the heterogeneous setup. These are opened questions calling for future studies.

5. Conclusions

We have considered transport in a doublet-type configuration through a heterogeneous porous formation. Unlike previous (both analytical and numerical) studies, we have developed a model accounting for transport even in the intermediate zone between the injecting and the pumping well. In this way, one can follow the behavior of the solute propagation, besides monitoring the BTC at the recovery (pumping) well.

The huge difficulty of this problem is the strong coupling of the nonuniformity of the flow with the spatial variability of the log-conductivity Y, an issue which limits enormously adoption of numerical methods. That is why simple (analytical) solutions, although mathematically cumbersome, are to be preferred. We have adopted a stochastic Lagrangian framework, based upon the travel time-formulation, to replace a three-dimensional reactive transport equation with a one-dimensional equation. To contain the mathematical burden (while retaining the most relevant features of the problem at stake), a few simplifying assumptions have been adopted: (a) the log-conductivity Y is modeled as a Gaussian, stationary, random field of axisymmetric anisotropy; (b) an asymptotic expansion, accurate at the first order in the variance σ_Y^2 and in the anisotropy ratio λ, of the velocity field is employed; (c) wells are fully penetrating with length much larger than the vertical integral scale in order to fulfill ergodicity; (d) pore-scale dispersion is neglected. For illustration purposes, a fairly general solution for a solute undergoing a first-order kinetics is considered.

Central for the present study is the computation of the PDF (Equation 34) of the travel time, which is derived similarly to Severino et al. (2012). In particular, it requires the computation of the mean (Equation 22), and (cross)-variances (Equations 23 and 24) along different streamlines delivered at the injecting well, and intersecting a CP at any position x_1 perpendicular to the distance 2ℓ between the two wells. In particular, moments of the travel time coincide with the expressions obtained by Koplik et al. (1994) and Dagan and Indelman (1999) when the CP is placed right at the pumping well. Hence, one can compute the flux-averaged concentration (BTC) both at the pumping well (similarly to Dagan and Indelman (1999) and Zech et al. (2018)) as well as at any CP in the intermediate zone between the two wells. Overall, the effect of sorption upon the BTC is manifested in the existence of a wake of solute trailing behind the propagating pulse. This wake is represented by the second term of Equation 36. At aquifer scale, the heterogeneity in the convective mechanism produces a further separation into parcels that move quicker than the mean through zones of higher permeability, with the opposite occurring in low-conductivity regions. Finally, the model is applied to a couple of field-scale transport experiments. In particular, they are used to identify the horizontal integral scale of the hosting formations. With such a parameter, and the knowledge of the variance σ_Y^2, we elucidate the main features of the transport developing in the intermediate zone delimited by the two wells. Other potential applications of the developed model are also outlined.

The present study can be generalized along several directions. Accounting for a formation with a high degree (i.e., large σ_Y^2) of heterogeneity is by far the most important of them, due to its relevance toward the analysis of field-scale transport experiments (see, e.g., Bianchi et al., 2011).

Declaration

Although the exploited information is contained in the provided figures and in the paper of Zech et al. (2018), upon acceptance of the manuscript, the full data set will be made available in an ad hoc repository (https://doi.org/10.5281/zenodo.5773764).

Conflict of Interest

The authors declare no conflicts of interest relevant to this study.

Acknowledgments
The authors express their gratitutde to Alraune Zech, Claudia D'Angelo, Sabine Attinger, and Aldo Fiori for providing the data set concerning the experiments at the Mobile and Barstow aquifers. The authors are indebted to the Editor-in-Chief (Xavier Sanchez-Vila) and to the Associate Editor (Alberto Bellin) for their fruitful suggestions. Finally, the authors thank Matteo Icardi and an anonymous Reviewer for their comments, which have improved the early version of the manuscript. Open Access Funding provided by Universita degli Studi di Napoli Federico II within the CRUI-CARE Agreement.

References

Bellin, A., Severino, G., & Fiori, A. (2011). On the local concentration probability density function of solutes reacting upon mixing. *Water Resources Research*, *47*, W01514. https://doi.org/10.1029/2010WR009696

Bianchi, M., Zheng, C., Tick, G. R., & Gorelick, S. M. (2011). Investigation of small-scale preferential flow with a forced-gradient tracer test. *Groundwater*, *49*(4), 503–514. https://doi.org/10.1111/j.1745-6584.2010.00746.x

Bruggeman, G. A. (1999). *Analytical solutions of geohydrological problems*. Elsevier.

Cvetkovic, V., & Dagan, G. (1994). Transport of kinetically sorbing solute by steady random velocity in heterogeneous porous formations. *Journal of Fluid Mechanics*, *265*, 189–215. https://doi.org/10.1017/S0022112094000807

Dagan, G. (1989). *Flow and transport in porous formation*. Springer-Verlag.

Dagan, G., & Indelman, P. (1999). Reactive solute transport in flow between a recharging and a pumping well in a heterogeneous aquifer. *Water Resources Research*, *35*(12), 3639–3647. https://doi.org/10.1029/1999WR900214

Di Dato, M., de Barros, F. P., Fiori, A., & Bellin, A. (2018). Improving the efficiency of 3-D hydrogeological mixers: Dilution enhancement via coupled engineering-induced transient flows and spatial heterogeneity. *Water Resources Research*, *54*, 2095–2111. https://doi.org/10.1002/2017WR022116

Fernández-Garcia, D., Illangasekare, T. H., & Rajaram, H. (2004). Conservative and sorptive forced-gradient and uniform flow tracer tests in a three-dimensional laboratory test aquifer. *Water Resources Research*, *40*, W10103. https://doi.org/10.1029/2004WR003112

Fiori, A., & Dagan, G. (2000). Concentration fluctuations in aquifer transport: A rigorous first-order solution and applications. *Journal of Contaminant Hydrology*, *45*(1), 139–163. https://doi.org/10.1016/S0169-7722(00)00123-6

Indelman, P., & Dagan, G. (1999). Solute transport in divergent radial flow through heterogeneous porous media. *Journal of Fluid Mechanics*, *384*, 159–182. https://doi.org/10.1017/S0022112098004078

Indelman, P., Lessoff, S., & Dagan, G. (2006). Analytical solution to transport in three-dimensional heterogeneous well capture zones. *Journal of Contaminant Hydrology*, *87*(1–2), 1–21. https://doi.org/10.1016/j.jconhyd.2006.04.005

Koplik, J., Redner, S., & Hinch, E. (1994). Tracer dispersion in planar multipole flows. *Physical Review E*, *50*(6), 4650–4671. https://doi.org/10.1103/PhysRevE.50.4650

Kurowski, P., Ippolito, I., Hulin, J., Koplik, J., & Hinch, E. (1994). Anomalous dispersion in a dipole flow geometry. *Physics of Fluids*, *6*(1), 108–117. https://doi.org/10.1063/1.868075

Molz, F. J., Güven, O., Melville, J. G., Crocker, R. D., & Matteson, K. T. (1986). Performance, analysis, and simulation of a two-well tracer test at the mobile site. *Water Resources Research*, *22*(7), 1031–1037. https://doi.org/10.1029/WR022i007p01031

Ptak, T., Piepenbrink, M., & Martac, E. (2004). Tracer tests for the investigation of heterogeneous porous media and stochastic modelling of flow and transport—A review of some recent developments. *Journal of Hydrology*, *294*(1–3), 122–163. https://doi.org/10.1016/j.jhydrol.2004.01.020

Robson, S. G. (1974). *Feasibility of digital water-quality modeling illustrated by application at Barstow, California (Tech. Rep.)*. US Geological Survey: Water Resources Division.

Rubin, Y. (2003). *Applied stochastic hydrogeology*. Oxford University Press.

Severino, G. (2011). Stochastic analysis of well-type flows in randomly heterogeneous porous formations. *Water Resources Research*, *47*, W03520. https://doi.org/10.1029/2010WR009840

Severino, G. (2022). Dispersion in doublet-type flows through highly anisotropic porous formations. *Journal of Fluid Mechanics*, *931*(A3), 1–13. https://doi.org/10.1017/jfm.2021.929

Severino, G., Cvetkovic, V., & Coppola, A. (2005). On the velocity covariance for steady flows in heterogeneous porous formations and its application to contaminants transport. *Computational Geosciences*, *9*(4), 155–177. https://doi.org/10.1007/s10596-005-9005-3

Severino, G., De Bartolo, S., Toraldo, G., Srinivasan, G., & Viswanathan, H. (2012). Travel time approach to kinetically sorbing solute by diverging radial flows through heterogeneous porous formations. *Water Resources Research*, *48*, W12527. https://doi.org/10.1029/2012WR012608

Severino, G., & Indelman, P. (2004). Analytical solutions for reactive transport under an infiltration-redistribution cycle. *Journal of Contaminant Hydrology*, *70*(1), 89–115. https://doi.org/10.1016/j.jconhyd.2003.08.007

Severino, G., Monetti, V., Santini, A., & Toraldo, G. (2006). Unsaturated transport with linear kinetic sorption under unsteady vertical flow. *Transport in Porous Media*, *63*(1), 147–174. https://doi.org/10.1007/s11242-005-4424-0

Severino, G., Santini, A., & Sommella, A. (2011). Macrodispersion by diverging radial flows in randomly heterogeneous porous media. *Journal of Contaminant Hydrology*, *123*(1), 40–49. https://doi.org/10.1016/j.jconhyd.2010.12.005

Zech, A., D'Angelo, C., Attinger, S., & Fiori, A. (2018). Revisitation of the dipole tracer test for heterogeneous porous formations. *Advances in Water Resources*, *115*, 198–206. https://doi.org/10.1016/j.advwatres.2018.03.006